Neurobiology of Disease

Progressively Decreased HCN1 Channels Results in Cone Morphological Defects in Diabetic Retinopathy

Ruyi Han,[1,2,3] Mengmeng Jin,[4,5] Gezhi Xu,[1,2,3] and Jie He[4]

[1]Department of Ophthalmology, Eye, ENT Hospital of Fudan University, Shanghai, 200031, China, [2]Shanghai Key Laboratory of Visual Impairment, Restoration, Fudan University, Shanghai, 200031, China, [3]NHC Key Laboratory of Myopia, Fudan University, Shanghai, 200031, China, [4]State Key Laboratory of Neuroscience, Institute of Neuroscience, Shanghai Institutes for Biological Sciences, Center for Excellence in Brain Science and Intelligence Technology, Chinese Academy of Sciences, Shanghai, 200031, China, and [5]University of Chinese Academy of Sciences, Beijing, 100049, China

Historically, diabetic retinopathy has been recognized as a vascular disease. Recent clinical evidence suggests the initiation of diabetic retinopathy with neuropathy rather than microangiopathy. However, the molecular mechanism that drives diabetic retinopathy-associated neuropathy remains mostly unexplored. Here, we reported progressive diabetic retinopathy defects in blood glucose levels, shortening of cone segments and uncoupled appearance of retinal vascular abnormalities from *pdx1*$^{+/-}$ *mutants* zebrafish to glucose-treated *pdx1*$^{+/-}$ *mutants* zebrafish of both sexes. Further single-cell transcriptomic analysis revealed cones as the most vulnerable retinal neuron type that underwent three developmentally progressive cell states (States 1-3), predominantly present in WT animals, *pdx1*$^{+/-}$ *mutants*, and glucose-treated *pdx1*$^{+/-}$ *mutants*, respectively. Mechanistically, the expression of *hcn1* was progressively decreased in cones during its transition from State 1 to State 3. Furthermore, genetic *hcn1* disruption resulted in similar cone segment defects found in the diabetic retinopathy model, suggesting the involvement of progressive *hcn1* reduction in diabetic retinopathy-associated cone defects. Thus, our study provided a vertebrate retina model representing progressive diabetic retinopathy defects and further gained new mechanistic insights into the cone morphologic defects as an early neuropathy in diabetic retinopathy.

Key words: **cone; diabetic retinopathy; *hcn1*; neuropathy**

Significance Statement

We create a vertebrate retina model representing the progressive diabetic retinopathy-associated defects using zebrafish. Further systematic single-cell transcriptome analysis reveals two novel cell states of cones in response to different levels of higher glucose and the progressive decrease of HCN1 channels as a mechanism underlying cone defects in diabetic retinopathy.

Introduction

Diabetic retinopathy (DR), a primary vision-threatening pathology in the retina, is one of the most common complications of diabetes mellitus (Antonetti et al., 2021). Historically, DR has been recognized as a vascular disease based on clinically visible microvascular alterations in the fundus (Antonetti et al., 2021). However, more recent studies suggest that the early stage of DR might be a neuropathy rather than microangiopathy, in which the pathology in the neural retina and functional alterations was confirmed before any detectable microvascular lesions (Stitt et al., 2016; Pan et al., 2021). The hallmarks of retinal neuropathy include retinal cell apoptosis, color defects, increased implicit time, and decreased amplitude of the photopic 30 Hz flicker response in electroretinograms (ERGs), which imply the cone dysfunction as an early neuropathy event in DR (Greenstein et al., 1990, 2004; Bearse et al., 2006). Mechanistically, *de novo* lipogenesis, nicotinamide adenine dinucleotide (NAD^+), inflammation, and mitochondrial dysfunction have been involved in early diabetic neuroretinopathy. Rajagopal et al. (2021) showed an

Received Dec. 29, 2021; revised July 10, 2022; accepted Aug. 17, 2022.

Author contributions: R.H. and M.J. performed research; R.H. analyzed data; R.H. wrote the first draft of the paper; R.H. wrote the paper; G.X. and J.H. designed research; G.X. and J.H. edited the paper.

This work was supported by the Clinical Research Plan of SHDC SHDC2020CR2041B and Strategic Priority Research Program of Chinese Academy of Science Grant XDB32000000, and State Key Laboratory of Neuroscience. We thank Haiyan Wu and Lijuan Quan (FACS Facility at Institute of Neuroscience) for assistance with FACS; Dr. Min Zhang (Zhenning Zhou in Molecular and Cellular Biology Core Facility at the Institute of Neuroscience) for assistance with single-cell RNA-seq; Qian Hu, Yonghong Wang, and Yumei Zhang (Optical Imaging Facility at Institute of Neuroscience) for assistance with imaging; Huiwen Qin, Xia Tang, Hui Zhang, and Lei Du for assistance with single-cell sequencing data analysis; Mengmeng Jin, Shuguang Yu, and Xinling Jia for help with *in situ* hybridization; Mengmeng Jin and Huiwen Qin for help in single-cell dissociation; Xiaoying Qiu and Yingjie Ma for fish care; members of the J.H. laboratory for helpful discussion and suggestions; and China Zebrafish Resource Center for the support of transgenic zebrafish lines of *ins:mCherry* and *fli1a:EGFP*.

The authors declare no competing financial interests.

Correspondence should be addressed to Gezhi Xu at drxugezhi@163.com or Jie He at jiehe@ion.ac.cn.

https://doi.org/10.1523/JNEUROSCI.2550-21.2022

elevation of diabetes-associated retinal *de novo* lipogenesis in leptin receptor-deficient mice, whereas those with fatty acid synthase deletion in rods maintained preserved visual responses on induction of diabetes. Lin et al. (2016) reported that streptozotocin (STZ)-induced diabetic mice exhibited retinal NAD^+ deficiency, indicating the NAD^+ deficiency as underlying mechanisms for metabolic dysfunction and consequent photoreceptor (PR) cell death. Moreover, several studies (Du et al., 2013; Tonade et al., 2016) demonstrated that PR cells as major cell contributors in inflammatory mediator production in DR and PR deletion inhibited diabetes-induced increase in superoxide and inflammatory proteins (Du et al., 2013; Tonade et al., 2016). Ablation of neuronal *Glut1* ameliorated diabetes-induced reductions in ERG component amplitudes and prevented early elevations in retinal oxidative stress and inflammation (Holoman et al., 2021). These studies supported the early metabolic, consequent transcriptional and functional changes in PRs under hyperglycemia. However, the relationship between the early retinal neuropathy and vascular defects and molecular mechanisms responsible for early cone structural neuropathy still remain largely elusive.

Cones, whose segments are critical for visual acuity (Bringmann et al., 2018), exhibit remarkable structure changes in diabetic patients, including significantly decreased cone density, reduced thickness of the outer nuclear layer, and the loss of inner and outer segments (Lombardo et al., 2014; Boynton et al., 2015; Tan et al., 2015; Lammer et al., 2016; Tavares Ferreira et al., 2016, 2017; Wanek et al., 2016; Eliwa et al., 2018). In animal studies, diabetic mice and rats also showed the reduced PR cell density, the decreased outer nuclear layer thickness, and shortened outer segments in rods, M-cones, and S-cones (Park et al., 2003; Énzsöly et al., 2014; Fu et al., 2018). Zebrafish retinas are cone-dominated retinas composed of four PR classes, rods, UV-cones, blue-cones, and double-paired-cones (green- and red-detecting) (Viets et al., 2016). They provide an excellent vertebrate retina model to study cone neuropathy in DR. Induced by oscillating glucose levels for 30 d, hyperglycemic adult zebrafish (1 and 2 years old) showed morphologic degeneration of cone PRs and deficient cone-mediated ERGs (Alvarez et al., 2010). More recently, studies examined neural and vascular pathologies of pancreatic and duodenal homeobox 1 (*pdx1*)-mutated zebrafish from larval stages into adulthood and found the PRs dysfunction, clear capillary tortuosity, and hypersprouting, highlighting *pdx1 mutant* zebrafish as a valuable model to study the pathogenesis of DR (Ali et al., 2020; Wiggenhauser et al., 2020). However, the application of homozygous $pdx1^{-/-}$ is largely limited by the severely impaired survival of *mutants* into adulthood.

This study examined the retinal vascular morphologic abnormality and cone morphology alteration in glucose-treated WT animals, $pdx1^{+/-}$ *mutants*, and glucose-treated $pdx1^{+/-}$ *mutants*, and further investigated the underlying molecular mechanism for cone defects in $pdx1^{+/-}$ *mutants* and glucose-treated $pdx1^{+/-}$ *mutants*. $Pdx1^{+/-}$ *mutants* showed unaffected development into adulthood, but impaired glucose intolerance in adults and exhibited significant cone structural defects but without retinal vascular morphologic abnormality. The glucose treatment significantly increased the fasting blood glucose level of $pdx1^{+/-}$ *mutants* but not WT animals and exacerbated early DR phenotypes, including retinal vascular abnormalities. Further single-cell RNA sequencing (RNA-seq) analysis revealed that cones were the most vulnerable retinal neuron type in glucose-treated $pdx1^{+/-}$ *mutants*, in which the expression of *hcn1* (hyperpolarization-activated cyclic nucleotide-gated potassium channel 1) was gradually decreased in cones of $pdx1^{+/-}$ *mutants* and glucose-treated $pdx1^{+/-}$ *mutants*, compared with the WT. Furthermore, genetic disruption of *hcn1* resulted in severe damage of cone segments, recapitulating the cone morphologic alteration under hyperglycemia.

Materials and Methods

Zebrafish. Zebrafish embryos, larvae, and adults of either sex used in this study were produced, grown, and maintained at 28°C according to standard protocols. Published fishline lines used in this study include the following: AB (WT), Tg (*ins:mCherry*, ZDB-TGCONSTRCT-070124-2) (Pisharath et al., 2007), Tg (*fli1a:EGFP*, ZDB-TGCONSTRCT-070117-94) (Roman et al., 2002), and Tg (*lws2:nfsb-mcherry*) (S. Yu and He, 2019).

Mutant generation. Mutant generation was achieved via the CRISPR/Cas9 technique. For *pdx1* and *hcn1*, we designed one sgRNA targeting the first exon of *pdx1* and *hcn1*, respectively. The template for *in vitro* transcription of sgRNA was generated by amplification DNA fragment with sgRNA scaffold using a forward targeting primer and a reverse primer (Roman et al., 2002). The sgRNA was transcribed via MEGAscript T7 Transcription Kit (Invitrogen, AM1334) and purified using the LiCl precipitation approach. The sgRNA (100 ng/μl) and Cas9 protein (400 ng/µl; Novoprotein, E365-01A) was injected into one-cell-stage embryos. Positive *mutants* were screened by genotyping via Sanger sequencing of PCR products. *Pdx1* sgRNA forward primer: 5′-TAATACGACTCACTATAGGCATCTCTACAGTCGCTCGGTTTTAGAGCTAGAAATAGC-3′. *Pdx1* genotyping forward primer: 5′-cgcctcaccattgggc-3′. *Pdx1* genotyping reverse primer: 5′-atgcgtgcgtgtgagatttg-3′. *Hcn1* sgRNA forward primer: 5′-TAATACGACTCACTATAGGGTTTATGCAGCGGCAATTGTTTTAGAGCTAGAAATAGC-3′. *Hcn1* genotyping forward primer: 5′-gatcctgaagaacagcatgggg-3′. *Pdx1* genotyping reverse primer: 5′-ccaatatccagccgtctgcac-3′.

In vivo *confocal microscopy.* Five dpf Tg(*ins:mCherry*) larvae were anesthetized with 0.04% MS-222 (tricaine mesylate, Sigma-Aldrich, A5040) in ddH_2O and embedded in 0.5% low-melting-point agarose (Sigma-Aldrich, A0701) dissolved in ddH_2O for visualization on an inverted confocal microscope system (FV1200, Olympus) confocal microscope using 20× objective. Adult zebrafish were killed with 0.4% MS-222 in ddH_2O. After the removal of covered tissue, the pancreas was exposed and imaged under fluorescence microscope using 2.5× objective (MVX10, Olympus). The pancreas islet was quantified using ImageJ.

Blood glucose measurement. Adult zebrafish were fasted overnight and anesthetized with 0.04% MS-222. Wet weights were recorded and blood glucose was determined via FreeStyle Optium Neo glucose meter (Abbott) and measured as in a previous study (Zang et al., 2015).

Tissue preparation and immunostaining. The immunostaining was performed as in a previous protocol (S. Yu and He, 2019). In brief, tissue frozen sections were incubated with primary antibody at 4°C overnight and then incubated with AlexaFluor-488-, 594-, or 647-conjugated secondary antibody (1:1000; Jackson ImmunoResearch Laboratories) at room temperature for 2 h and DAPI for 8 min at room temperature. For retina flat mount, after penetration with 0.05% Triton in 1× PBS at 4°C for 24 h, fixed retina tissues were incubated with primary antibody at 4°C for 24 h and then incubated with secondary antibody at 4°C for 24 h. Primary antibodies are as follows: mouse monoclonal anti-Arrestin 3 antibody (Abcam, ab174435); mouse monoclonal anti-Rhodopsin antibody (Abcam, ab98887); rabbit cleaved Caspase3 antibody (Cell Signaling Technology, 9661T); and rabbit polyclonal anti-Glut1 antibody (Novus, NB300-666).

TUNEL staining. TUNEL staining was achieved via In Situ Cell Death Detection Kit (TMR red, Roche, 12156792910). Tissue sections were prepared as described as above. Frozen sections of positive control were treated with DNase-I solution for 30 min at 37°C. Staining procedures were performed according to manual protocol.

Single-cell sample preparation. Retina single-cell suspension was prepared according to a previous protocol (S. Yu and He, 2019). In brief, in each group (WT, $pdx1^{+/-}$, glucose-treated $pdx1^{+/-}$), six retinas from six

zebrafish were dissected and dissociated with 1 ml papain solution at 37°C for 15 min. The cell solution was further filtered with a 40 mm cell strainer (BD Falcon), incubated with Hoechst on ice for 5 min and centrifuged at 4°C for 5 min, discarded the supernatant, and added 600 μl washing buffer. FACS was performed and the Hoechst-labeled alive cells were collected.

Single-cell RNA-seq. A total of 5000-16000 cells were loaded onto the Chromium Single Cell Chip (10× Genomics) according to the manufacturer's protocol. The library was generated via Single Cell 3′ Library and Gel Bead kit version 3.1 Chip kit (10× Genomics, 120237) according to the manual protocol. Library quantification and quality assessments were achieved by Qubit fluorometric assay (Invitrogen) and the fragment analyzer with High Sensitivity Large Fragment 50 kb Analysis Kit (AATI, DNF-464). The indexed library was sequenced by the Illumina NovaSeq 6000 Sequencer with the S2 flow cell using paired-end 150 mode.

Single-cell RNA-seq data analysis. Single-cell FASTQ sequencing reads were processed and converted to digital gene expression matrices against the zebrafish genome (Zv11) by the Cell Ranger Software (version 3.1.0). An average of 33,509 reads and 890 detectable genes per cell was obtained. R packages (Seurat 3) were used for further analysis (http://satijalab.org/seurat/). After filtering low-abundance genes, cell doublets and low-quality libraries (with low gene numbers and high mitochondrial transcripts), retina cells from three groups (WT, *pdx1*$^{+/-}$, glucose-treated *pdx1*$^{+/-}$) were integrated. Integrated data were normalized, scaled, and clustered based on the principal gene components with a p value <0.001 (FindClusters, resolution = 0.6), which generated 39 clusters. *Pdx1* gene was not expressed by differentiated retinal cells. Cell identities of each cluster were annotated with putative retina cell markers in UMAP plot (see Fig. 4*C*). The cell numbers of endothelial cells (ECs) and macrophage/microgia (Mac/mic) in each sample were too low to do further subclustering analysis (ECs in WT: 36, ECs in *pdx1*$^{+/-}$ *mutants*: 5, ECs in glucose-treated *pdx1*$^{+/-}$ *mutants*: 34; Mac/mic in WT: 26, Mac/mic in *pdx1*$^{+/-}$ *mutants*: 11, Mac/mic in glucose-treated *pdx1*$^{+/-}$ *mutants*: 7). The gene–gene correlation was achieved with 'bioDist' R package according to pairwise Pearson correlational distances. Trajectory analysis was performed to investigate the pseudotime transcriptomic change of Clusters 2 and 6 by using 'monocle 2' R package, which revealed three distinct states (see Fig. 5*D*). Significantly differentially expressed genes among three states were determined with a p value <1e-4. Differently expressed genes were assigned into DAVID Bioinformatics Resources 6.8 (https://david.ncifcrf.gov) to achieve Gene Ontology (GO) analysis. Enriched GO biological process term with a p value <0.01 were annotated in Figure 5*G*.

ISH. The digoxigenin (DIG)-labeled *hcn1* antisense probe was synthesized by MEGAscriptTM T7 High Yield Transcription Kit (Invitrogen, AM1334) and DIG RNA labeling kit (Roche, 11277073910) according to the manual. The cDNA template was amplified by PCR with following primers: *Hcn1*-F: 5′-CCCGCTCAAAGAGGAAATTGTG-3′; *Hcn1*-R: 5′-TAATACGACTCACTATAGGGGAGAAACGCTCGGTGCTG-3′. ISH was performed according to the previous protocol (S. Yu and He, 2019). Briefly, on first day, sections were incubated with 1 μg/ml probe at 60°C overnight. On the second day, slides were incubated in TNB buffer with anti–DIG-POD (1:500; Roche) at 4°C overnight. On the third day, the signal was detected by the TSATM Plus Cyanine 3/Fluorescein System (PerkinElmer, NEL753001KT).

Quantification. All quantification was performed with FV10-ASW 4.0 Viewer (Olympus), FV31S-SW (Olympus), and ImageJ. For pancreas islet area measurement, all data were automatically measured by limit to color threshold in ImageJ. For retinal vessel sprouts and branches quantification, whole retina vessel images were automatically stitched via the inverted confocal microscope system (FV3000, Olympus). FV31S-SW (Olympus) was used for visualization and quantification. Capillary plexus was defined as higher than fourth vessel branch. The area with the width in 350 μm was defined as a unit area. Arterial density per eye was quantified by calculating the vessel signal area divided by total pixel area in four regions (350 μm^2) from individual retina in ImageJ, and arterial diameter per eye was measured in 4-9 first branched artery by ImageJ. For *glut1* fluorescence intensity, stitching retinal vessel images were stacked in Z projection with max intensity, and mean gray value was quantified in at least four regions (350 μm^2) in individual retina by ImageJ. For cell number quantification, sections with optic nerve were selected and quantified. The cell number in three or more regions of width in 50 μm were counted as the average cell number in the eye. RGB (red, green, blue) cones, UV cones, and rods were recognized by the nuclear location and the nuclear density. For cone segment quantification, >3 sequential regions of width in 210 μm were taken per eye and 5 times measurements were done per region. Thus, the average of cone segments length in 15 or more site was determined as the cone segments in one eye. *Hcn1 in situ* signal fluorescence intensity was automatically measured by limit to color threshold in at least three or more regions per eye by ImageJ. Area fraction was quantified by calculating the signal area divided by total pixel area of cone layer in at least three or more regions per eye by ImageJ.

Statistics. All data are presented as the mean ± SD from at least three independent experiments. Statistical comparisons between two groups were analyzed by two-tailed unpaired Student's t test, two-tailed unpaired Welch's t test, or ratio paired t test, according to the homogeneity of variances and normal distribution using GraphPad Prism 9 (GraphPad Software). Statistical significance was defined as a p value of <0.05.

Study approval. Animal procedures performed in this study were approved by the Animal Use Committee of Institute of Neuroscience, Chinese Academy of Sciences (NA-045-2019).

Data and resource availability statements. The datasets generated during and/or analyzed during the current study are available from the corresponding author on reasonable request.

Results

Pdx1$^{+/-}$ *mutants* and glucose-treated *pdx1*$^{+/-}$ *mutants* result in different high glucose levels in adult zebrafish

Pdx1 gene is essential for the development of the pancreas, which maintains the homeostasis of glucose levels (Wiggenhauser et al., 2020). To create a zebrafish model for DR, we injected the sgRNA targeting the *pdx1* exon 1 and Cas9 protein into embryos at one-cell stage. After F2 generation, animals with a frame-shift mutation were selected for experiments. Although *pdx1*$^{-/-}$ homozygote *mutants* were lethal starting at 5 d post-fertilization (pdf), *pdx1*$^{+/-}$ heterozygote *mutants* showed an unaffected development into adulthood. We first characterized the size of the pancreas islet in *pdx1*$^{+/-}$ *mutants* by crossing it with Tg(*ins:mCherry*), the transgenic line specifically labeling pancreatic β cells. We found that the pancreas islet mass of *pdx1*$^{+/-}$ *mutants* was significantly less in size than that of the WT at 5 dpf and the adulthood (Fig. 1*A–D*; at 5 dpf: WT 923.6 ± 316.8 μm^2, n = 36; *pdx1*$^{+/-}$ *mutants*, 689.4 ± 231.2 μm^2, n = 22; p = 0.0039, by two-tailed unpaired Student's t test; at adult: WT 311,847.0 ± 97,170.0 μm^2, n = 7; *pdx1*$^{+/-}$ *mutants*, 176,355 ± 53,093.0 μm^2, n = 9; p = 0.0030, by two-tailed unpaired Student's t test), which was consistent with previous studies (Ali et al., 2020; Wiggenhauser et al., 2020). The finding of decreased pancreas' size indicated the deficits in pancreatic β cell development.

Next, we measured the fasting blood glucose level in *pdx1*$^{+/-}$ *mutants* at 3 months post-fertilization (mpf). We found that the fasting blood glucose level of *pdx1*$^{+/-}$ *mutants* was significantly higher than that of the WT (Fig. 1*F*; WT, 60.2 ± 25.2 mg/dl, n = 36; *pdx1*$^{+/-}$ *mutants*, 75.4 ± 29.9 mg/dl, n = 31; p = 0.027, by two-tailed unpaired Student's t test), indicating the defect in glucose tolerance of adult *pdx1*$^{+/-}$ *mutants*.

To further evaluate the influence of the glucose administration on the blood glucose level of *pdx1*$^{+/-}$ adult *mutants*, we applied a 2 week glucose treatment to 2.5 mpf *pdx1*$^{+/-}$ *mutants* (Fig. 1*E*). The fasting blood glucose level of glucose-

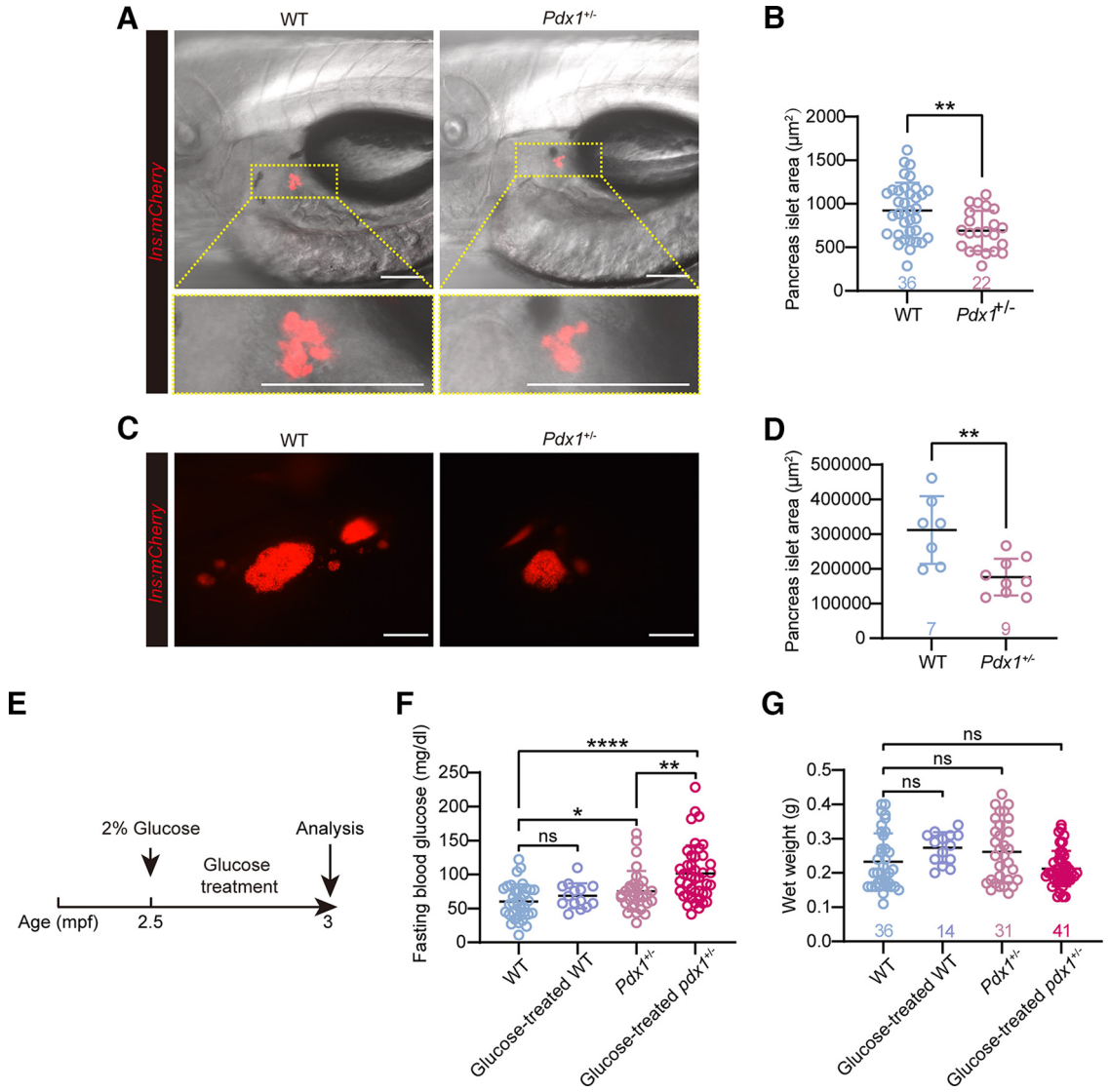

Figure 1. Different high blood glucose levels in adult *pdx1*$^{+/-}$ *mutants* and glucose-treated *pdx1*$^{+/-}$ *mutants*. ***A***, Representative confocal microscopic images of pancreatic β cells in WT and *pdx1*$^{+/-}$ *mutants* in Tg(*ins:mCherry*) at 5 dpf. Scale bars, 100 μm. ***B***, Pancreas islet mass of 5 dpf WT and *pdx1*$^{+/-}$ *mutants*, quantified by the fluorescence labeled area. Data are mean ± SD. WT, $n = 36$; *pdx1*$^{+/-}$ *mutants*, $n = 22$. $^{**}p < 0.01$ (two-tailed unpaired Student's *t* test). ***C***, Representative confocal microscopic images of pancreatic β cells in adult WT and *pdx1*$^{+/-}$ *mutants* in Tg(*ins:mCherry*). Scale bars, 2400 μm. ***D***, Pancreas islet mass of adult WT and *pdx1*$^{+/-}$ *mutants*, quantified by the fluorescence labeled area. Data are mean ± SD. WT, $n = 7$; *pdx1*$^{+/-}$ *mutants*, $n = 9$. $^{**}p < 0.01$ (two-tailed unpaired Student's *t* test). ***E***, Experimental design: 2.5 mpf *pdx1*$^{+/-}$ *mutants* received 2% glucose treatment for 14 d. ***F***, The fasting blood glucose levels of WT, glucose-treated WT, *pdx1*$^{+/-}$ *mutants*, and glucose-treated *pdx1*$^{+/-}$ *mutants* at 3 mpf. Data are mean ± SD. WT, $n = 36$; glucose-treated WT, $n = 14$; *pdx1*$^{+/-}$ *mutants*, $n = 31$; glucose-treated *pdx1*$^{+/-}$ *mutants*, $n = 41$. NS ($p > 0.05$); $^{*}p < 0.05$; $^{**}p < 0.01$; $^{****}p < 0.0001$; two-tailed unpaired Student's *t* test or two-tailed unpaired Welch's *t* test. ***G***, The wet weights of WT, glucose-treated WT, *pdx1*$^{+/-}$ *mutants*, and glucose-treated *pdx1*$^{+/-}$ *mutants* at 3 mpf. Data are mean ± SD. WT, $n = 36$; glucose-treated WT, $n = 14$; *pdx1*$^{+/-}$ *mutants*, $n = 31$; glucose-treated *pdx1*$^{+/-}$ *mutants*, $n = 41$. NS ($p > 0.05$) (two-tailed unpaired Student's *t* test or two-tailed unpaired Welch's *t* test; see Extended Data Fig. 1-1). Exemplary sequence result of mutation in *pdx1* exon 1.

treated *mutants* (101.6 ± 41.2 mg/dl, $n = 41$) was 1.3-fold and 1.7-fold higher than that of *pdx1*$^{+/-}$ *mutants* (75.4 ± 29.9 mg/dl, $n = 31$, $p = 0.0036$, by two-tailed unpaired Student's *t* test) and WT animals (60.2 ± 25.3 mg/dl, $n = 36$, $p < 0.0001$, by two-tailed unpaired Welch's *t* test), respectively (Fig. 1*F*). Meanwhile, the wet weight of glucose-treated *mutants* (0.21 ± 0.05 g, $n = 41$) did show no significant change compared with that of WT (Fig. 1*G*; 0.23 ± 0.08 g, $n = 36$, $p = 0.2$, by two-tailed unpaired Welch's *t* test), excluding the contribution of the wet weight to increased glucose levels in glucose-treated *pdx1*$^{+/-}$ *mutants*. However, the fasting blood glucose level of glucose-treated WT (Fig. 1*F*; 68.6 ± 18.35 mg/dl, $p = 0.3$, by two-tailed unpaired Student's *t* test) did not show significant difference compared with WT animals, which demonstrated that 2 week glucose treatment did not induce hyperglycemia in WT zebrafish. Together, our results demonstrated that combining *pdx1*$^{+/-}$ *mutants* and glucose treatment could result in different high glucose levels in adult zebrafish, which could model progressive DR phenotypes.

Glucose-treated *pdx1*$^{+/-}$ *mutants* but not *pdx1*$^{+/-}$ *mutants* exhibit microvascular defects

To model progressive DR phenotypes using *pdx1*$^{+/-}$ *mutants* and glucose-treated *pdx1*$^{+/-}$ *mutants*, we focused on two key DR characteristics: microvascular defects and cone morphologic alteration.

In adult zebrafish, retinal vasculature is organized in a uniformed pattern, which initiates from the optic artery, and divides into 4-9 main artery vessels at the optic disk (Ali et al., 2020).

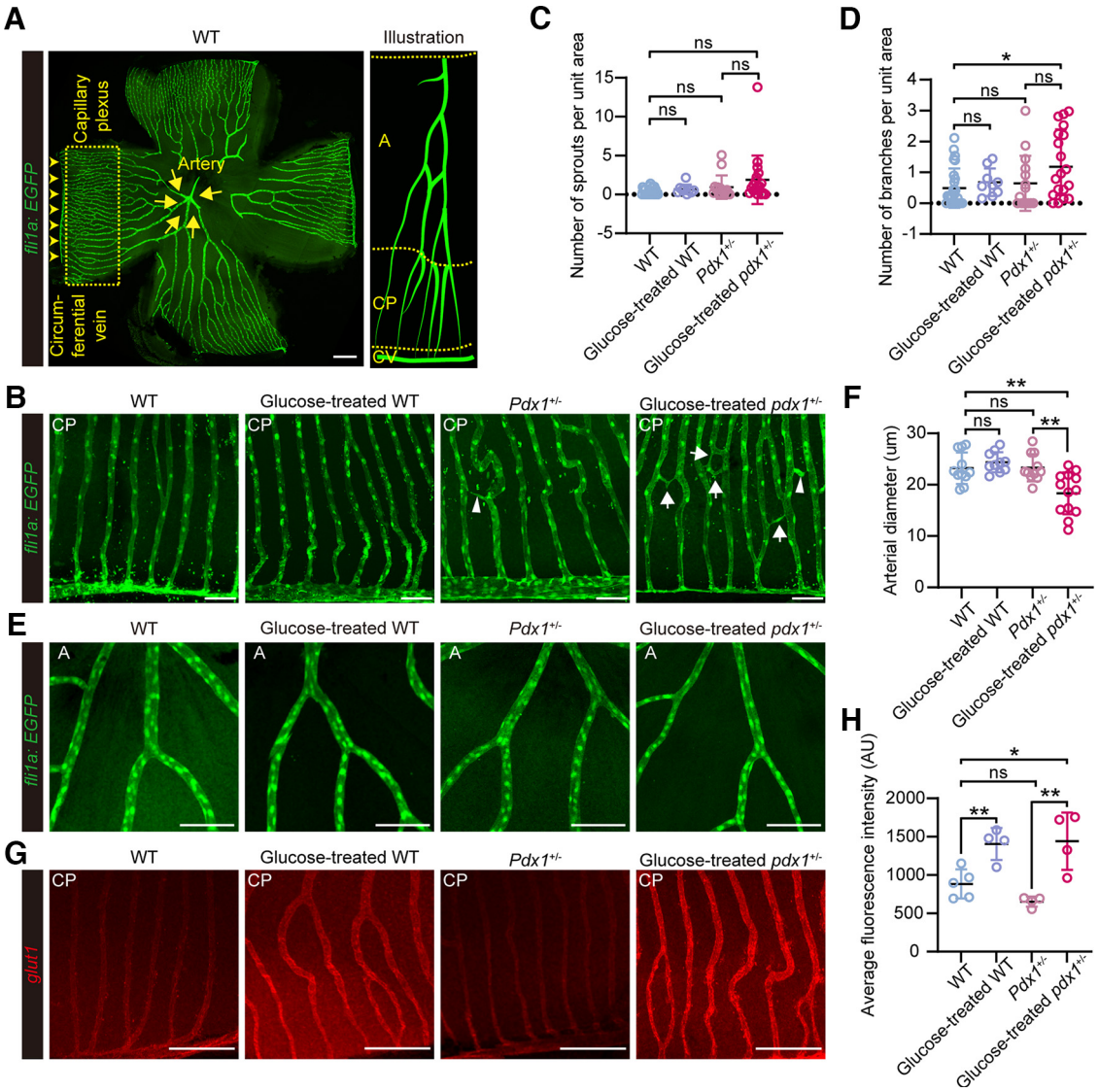

Figure 2. Retinal vascular abnormalities in adult glucose-treated *pdx1*$^{+/-}$ *mutants*. ***A***, Representative image of WT zebrafish retinal vasculature in Tg(*fli1a:EGFP*) at 3 mpf. Arrow indicates artery vessels (A). Dotted box represents capillary plexus (CP). Arrowhead indicates circumferential vein (CV). Scale bars, 200 μm. ***B***, Representative confocal microscopic images of retinal capillary plexus of WT, glucose-treated WT, *pdx1*$^{+/-}$, and glucose-treated *pdx1*$^{+/-}$ *mutants*. Arrow indicates branches. Arrowhead indicates sprouts. Scale bars, 50 μm. The number of sprouts (***C***) and branches (***D***) in capillary plexus of WT, glucose-treated WT, *pdx1*$^{+/-}$, and glucose-treated *pdx1*$^{+/-}$ *mutants* retinas. Data are mean ± SD. WT, $n = 26$ retinas from 17 animals; glucose-treated WT, $n = 9$ retinas from 6 animals; *pdx1*$^{+/-}$ *mutants*, $n = 15$ retinas from 12 animals; glucose-treated *pdx1*$^{+/-}$ *mutants*, $n = 19$ retinas from 11 animals. *$p < 0.05$; NS ($p > 0.05$); two-tailed unpaired Welch's *t* test. ***E***, Representative confocal microscopic images of retinal arteries of WT, glucose-treated WT, *pdx1*$^{+/-}$, and glucose-treated *pdx1*$^{+/-}$ *mutants*. Scale bars, 100 μm. ***F***, The arterial diameters of WT, glucose-treated WT, *pdx1*$^{+/-}$, and glucose-treated *pdx1*$^{+/-}$ mutant retinas. Data are mean ± SD. WT, $n = 11$ retinas from 7 animals; glucose-treated WT, $n = 10$ retinas from 10 animals; *pdx1*$^{+/-}$ *mutants*, $n = 11$ retinas from 8 animals; glucose-treated *pdx1*$^{+/-}$ *mutants*, $n = 13$ retinas from 8 animals. *$p < 0.05$; NS ($p > 0.05$); two-tailed unpaired Student's *t* test. ***G***, Representative confocal microscopic images of retinal capillary plexus in WT, glucose-treated WT, *pdx1*$^{+/-}$, and glucose-treated *pdx1*$^{+/-}$ *mutants* retinas stained by *glut1* antibody. Scale bars, 100 μm. ***H***, The average fluorescence intensity of *glut1* in retinal capillary plexus of WT, glucose-treated WT, *pdx1*$^{+/-}$, and glucose-treated *pdx1*$^{+/-}$ *mutants* retinas. Data are mean ± SD. WT, $n = 5$ retinas from 5 animals; glucose-treated WT, $n = 4$ retinas from 4 animals; *pdx1*$^{+/-}$ *mutants*, $n = 4$ retinas from 4 animals; glucose-treated *pdx1*$^{+/-}$ *mutants*, $n = 4$ retinas from 4 animals. **$p < 0.01$; NS ($p > 0.05$); two-tailed unpaired Student's *t* test (see Extended Data Fig. 2-1). Decreased retinal arterial density in adult glucose-treated *pdx1*$^{+/-}$ *mutants*.

The main artery vessels spread over retina's inner surface, arborize radially as progressively narrower vessels, and eventually anastomose with capillary plexus draining into the circumferential vein (Fig. 2*A*). Under the hyperglycemic condition, active angiogenesis in the microvasculature was temporally ahead of changes in other main blood vessels (Stitt et al., 2016).

We wondered the degree of microvascular abnormalities in glucose-treated adult WT, *pdx1*$^{+/-}$ adult *mutants*, and glucose-treated *pdx1*$^{+/-}$ adult *mutants*. The numbers of sprouts and branches of glucose-treated WT animals (0.7 ± 0.6 sprouts and 0.7 ± 0.4 branches per unit area, $n = 9$ retinas from 6 animals) did not significantly altered compared with that of WT animals (Fig. 2*B–D*; 0.4 ± 0.4 sprouts and 0.5 ± 0.6 branches per unit area, $n = 26$ retinas from 17 animals, $p = 0.1$ and 0.4, by two-tailed unpaired Student's *t* test). Also, the numbers of sprouts and branches of *pdx1*$^{+/-}$ *mutants* (0.9 ± 1.5 sprouts and 0.6 ± 0.9 branches per unit area, $n = 15$ retinas from 12 animals) did not show significant difference compared with those of WT animals (Fig. 2*B–D*; $p = 0.2$ and 0.5, by two-tailed unpaired Welch's *t* test and two-tailed unpaired Student's *t* test). However, compared with that of WT animals, the number of branches (1.2 ± 1.1 branches per unit area, $n = 19$ retinas from 11 animals, $p = 0.0185$,

by two-tailed unpaired Welch's *t* test) became significantly increased in glucose-treated *pdx1*$^{+/-}$ *mutants*, consistent with a recent study (Wiggenhauser et al., 2020), while still leaving the number of sprouts unchanged (Fig. 2*B–D*). Thus, our results showed a detectable level of active retina angiogenesis in glucose-treated *pdx1*$^{+/-}$ *mutants* but not in *pdx1*$^{+/-}$ *mutants*.

Previous studies also showed that retinal artery lesions occurred under hyperglycemia (Ali et al., 2020). We then looked into the diameter and density of retinal arteries. Similarly, the retinal arterial diameter and density of glucose-treated WT animals (arterial diameter, 24.38 ± 2.0 μm, $n = 10$ retinas from 10 animals, $p = 0.3$, by two-tailed unpaired Student's *t* test; arterial density, 14.1 ± 1.2%, $n = 9$ retinas from 9 animals, $p = 1.0$, by two-tailed unpaired Student's *t* test) did not significantly change compared with those of WT animals (Fig. 2*E*,*F*; arterial diameter, 23.2 ± 3.1 μm, $n = 11$ retinas from 7 animals; arterial density, 14.1 ± 1.0%, $n = 12$ retinas from 9 animals). Moreover, glucose-treated *pdx1*$^{+/-}$ *mutants* (arterial diameter, 18.3 ± 4.1 μm, $n = 13$ retinas from 8 animals, $p = 0.0034$, by two-tailed unpaired Student's *t* test; arterial density, 13.1 ± 1.2%, $n = 12$ retinas from 8 animals, $p = 0.0356$, by two-tailed unpaired Student's *t* test) but not *pdx1*$^{+/-}$ *mutants* (arterial diameter, 23.3 ± 2.7 μm, $n = 11$ retinas from 8 animals, $p = 0.9$, by two-tailed unpaired Student's *t* test; arterial density, 14.8 ± 1.5%, $n = 11$ retinas from 9 animals, $p = 0.2$, by two-tailed unpaired Student's *t* test) exhibited significantly decreased retinal arterial diameter and density compared with those of WT animals (Fig. 2*E*,*F*).

To further characterize microvasculature abnormalities at the molecular level, we examined the expression of *glut1*, a marker of healthy blood–retina barrier, which mediates the entry of glucose into ECs (Takagi et al., 1998; Kumagai et al., 1996). Surprisingly, although 2 week glucose treatment did not induce hyperglycemia or significant cellular vascular defects in young-adult WT zebrafish (Fig. 1*F*), the expression of *glut1* was significantly increased in glucose-treated WT animals (1442.0 ± 374.4 AU, $n = 4$ retinas from 4 animals) compared with that of WT animals (Fig. 2*G*,*H*; 884.1 ± 190.1 AU, $n = 5$ retinas from 5 animals, $p = 0.0058$, by two-tailed unpaired Student's *t* test). Similarly, glucose treatment in *pdx1*$^{+/-}$ *mutants* also induced significant upregulation of *glut1* (Fig. 2*G*,*H*; *pdx1*$^{+/-}$ *mutants*, 651.9 ± 66.71 AU, $n = 4$ retinas from four animals; glucose-treated *pdx1*$^{+/-}$ *mutants*, 1442.0 ± 374.4 AU, $n = 4$ retinas from four animals, $p = 0.0060$, by two-tailed unpaired Student's *t* test). However, compared with that of WT animals, the expression of *glut1* in *pdx1*$^{+/-}$ *mutants* did not significantly change (Fig. 2*G*,*H*; $p = 0.05$, by two-tailed unpaired Student's *t* test). These results showed that glucose treatment but not *pdx1* knockdown resulted in the molecular defect of retinal vasculature.

Pdx1$^{+/-}$ *mutants* and glucose-treated *pdx1*$^{+/-}$ *mutants* exhibit progressive cone morphologic defects

Next, we examined cone defects in *pdx1*$^{+/-}$ *mutants* and glucose-treated *pdx1*$^{+/-}$ *mutants*. We first examined whether cones were undergoing apoptosis using TUNEL staining in *pdx1*$^{+/-}$ *mutants* with or without glucose treatment. We did not observe apoptotic cells. In addition, the numbers of RGB cones and UV cones did not show any significant changes in glucose-treated WT, *pdx1*$^{+/-}$ *mutants*, and glucose-treated *pdx1*$^{+/-}$ *mutants* compared with WT animals (Fig. 3*A*,*B*). Additionally, we also did not observe the change in the cell number of rods or the cell number in the inner nuclear layer (INL) (Fig. 3*C*,*D*). Thus, there was no cone loss in *pdx1*$^{+/-}$ *mutants* with or without glucose treatment.

However, when looking into the detailed morphology of cone PRs, notably, we observed a significant decrease in the length of double-cone segments in *pdx1*$^{+/-}$ *mutants* compared with that of WT animals (WT, 29.9 ± 2.5 μm, $n = 19$ retinas from 10 animals; *pdx1*$^{+/-}$ *mutants*, 27.2 ± 2.5 μm, $n = 17$ retinas from 9 animals; WT vs *pdx1*$^{+/-}$ *mutants*, $p = 0.0029$, by two-tailed unpaired Student's *t* test), while the length of double-cone segments in glucose-treated WT animals (28.8 ± 2.2 μm, $n = 11$ retinas from 6 animals, $p = 0.3$, by two-tailed unpaired Student's *t* test) was statistically indistinguishable from that of WT animals (Fig. 3*E*,*F*). Moreover, the degree of double-cone segments shortening became more severe in glucose-treated *pdx1*$^{+/-}$ *mutants* (Fig. 3*E*,*F*; glucose-treated *pdx1*$^{+/-}$ *mutants*, 24.5 ± 2.5 μm, $n = 14$ retinas from 8 animals; with *pdx1*$^{+/-}$ *mutants*, $p = 0.0033$; with WT, $p < 0.0001$; by two-tailed unpaired Student's *t* test). To exclude the contribution of the developmental effects induced by *pdx1* knockdown to this decrease in double-cone segments, we further examined cell apoptosis, cell numbers, and the length of cone segments in 7 dpf zebrafish. Compared with those of WT animals, the cell apoptosis labeled by TUNEL and caspase3 staining, the number of cones and rods, and the length of cone segments were not significantly altered. Thus, our data indicated that increased blood glucose levels resulted in the progressive alteration of cone morphology in *pdx1*$^{+/-}$ *mutants* without and with glucose treatment.

Single-cell RNA-seq revealing the vulnerability of cones to high glucose levels

To understand the molecular mechanism underlying progressive cone structural alteration from *pdx1*$^{+/-}$ *mutants* to glucose-treated *pdx1*$^{+/-}$ *mutants*, we performed single-cell transcriptome analysis of retinal cells in *pdx1*$^{+/-}$ *mutants*, glucose-treated *pdx1*$^{+/-}$ *mutants*, and WT animals using the 10× Genomics platform (Fig. 4*A*). We obtained a total of 15,051 qualified single-cell transcriptomes (8142 cells, WT; 2994 cells, *pdx1*$^{+/-}$ *mutants*; 3915 cells, glucose-treated *pdx1*$^{+/-}$ *mutants*) with an average of 890 detectable genes per cell. According to gene expression profiles, all retina cells were segregated into 39 clusters in the UMAP plot. Based on the expression of putative retinal cell type-specific marker genes (Fig. 4*B*), we characterized cell identities of 33 clusters, including PR cells, bipolar cells, amacrine cells, retinal ganglion cells, Müller cells (MCs), macrophage/microglia cells, and ECs (Fig. 4*C*). The retinas of all three groups exhibited statically indistinguishable in terms of cell-type composition (Fig. 4*D*) (WT vs *pdx1*$^{+/-}$ *mutants*, $p = 0.7$; WT vs glucose-treated *pdx1*$^{+/-}$ *mutants*, $p = 0.8$; by ratio paired *t* test; *pdx1*$^{+/-}$ *mutants* vs glucose-treated *pdx1*$^{+/-}$ *mutants*, $p = 0.6$; by ratio paired *t* test).

Furthermore, we compared the compositions of cell clusters assigned to each major retinal cell type among three groups (WT, *pdx1*$^{+/-}$ *mutants*, and glucose-treated *pdx1*$^{+/-}$ *mutants*). Remarkably, PR clusters showed the notable change in composition (Fig. 4*E*,*F*). Of 15 PR clusters, Cluster 2 cells were predominantly present in both WT and *pdx1*$^{+/-}$ *mutants* (13.6% and 23.5% of total PRs in WT and *pdx1*$^{+/-}$ *mutants*, respectively), but mostly absent from glucose-treated *pdx1*$^{+/-}$ *mutants* (only 0.6% of total PRs) (Fig. 4*E*,*F*). However, Cluster 6 cells mainly were identified in glucose-treated *pdx1*$^{+/-}$ *mutants*, accounting for nearly 20.4% in all PRs, but largely absent from WT and *pdx1*$^{+/-}$ *mutants* (Fig. 4*E*,*F*). These results indicated that PRs were vulnerable to hyperglycemia among all retinal neurons.

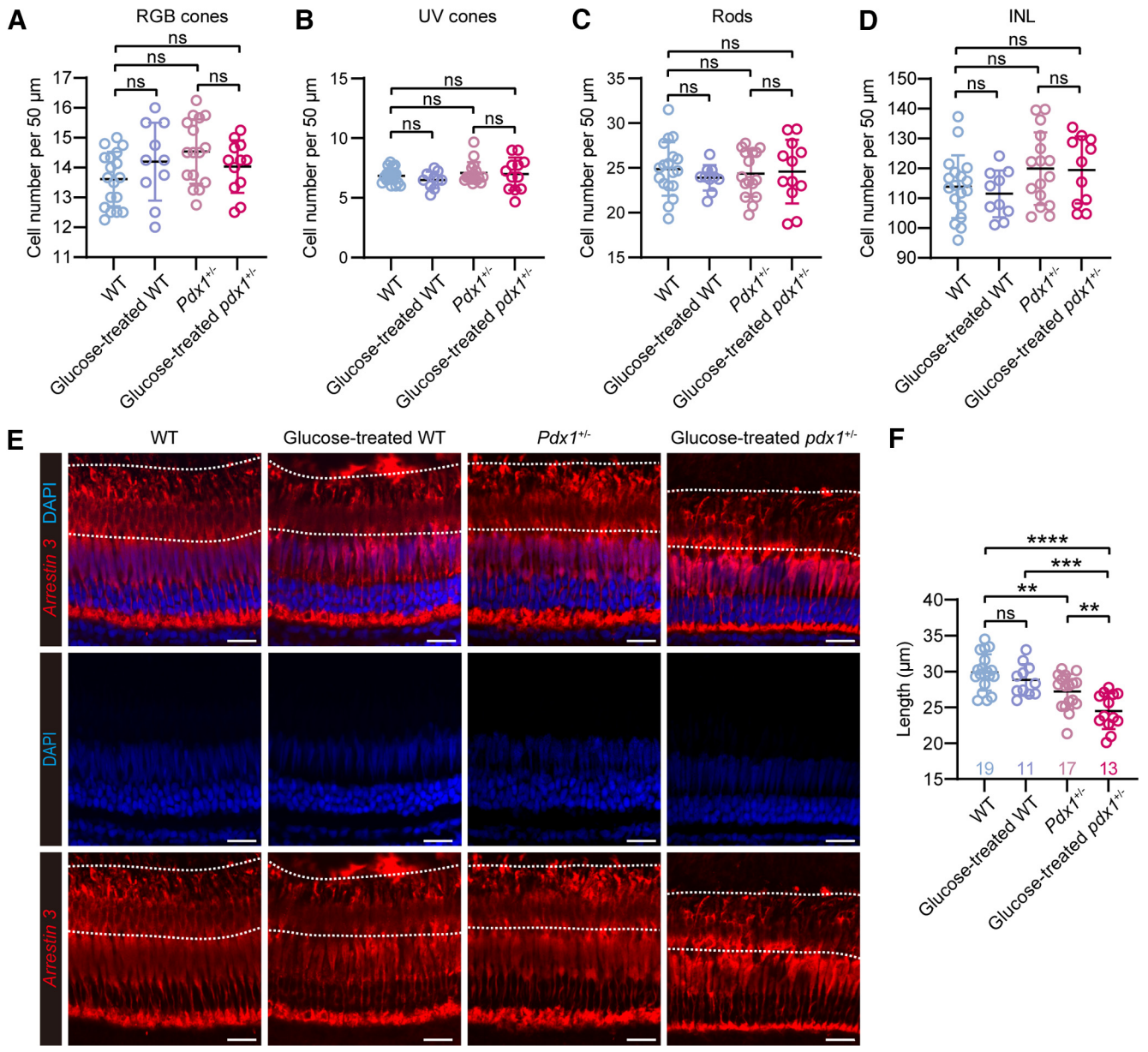

Figure 3. Progressive cones morphologic defects in *pdx1*$^{+/-}$ *mutants* and glucose-treated *pdx1*$^{+/-}$ *mutants*. The cell numbers of RGB cones (***A***), UV cones (***B***), rods (***C***), and cell number in INL (***D***) in 3 or more regions of width 50 µm per eye of WT, *pdx1*$^{+/-}$, and glucose-treated *pdx1*$^{+/-}$ *mutants* retinas at 3 mpf. Data are mean ± SD. WT, $n = 18$ retinas from 10 animals; glucose-treated WT, $n = 10$ retinas from 6 animals; *pdx1*$^{+/-}$ *mutants*, $n = 16$ retinas from 8 animals; glucose-treated *pdx1*$^{+/-}$ *mutants*, $n = 12$ retinas from 7 animals. NS, $p > 0.05$ (two-tailed unpaired Student's *t* test or two-tailed unpaired Welch's *t* test). ***E***, Representative confocal microscopic images of double-cones in WT, glucose-treated WT, *pdx1*$^{+/-}$, and glucose-treated *pdx1*$^{+/-}$ *mutants*. Dotted lines indicate cone segments. Scale bars, 15 µm. ***F***, The length of cone segments in 15 or more regions per eye. Data are mean ± SD. WT, $n = 19$ retinas from 10 animals; glucose-treated WT, $n = 11$ retinas from 6 animals; *pdx1*$^{+/-}$ *mutants*, $n = 17$ retinas from 9 animals; glucose-treated *pdx1*$^{+/-}$ *mutants*, $n = 14$ retinas from 8 animals. NS ($p > 0.05$); $^{**}p < 0.01$; $^{***}p < 0.001$; $^{****}p < 0.0001$; two-tailed unpaired Student's *t* test (see Extended Data Fig. 3-1). No cell apoptosis in *pdx1*$^{+/-}$ *mutants* and glucose-treated *pdx1*$^{+/-}$ *mutant* retinas (see Extended Data Fig. 3-2). Illustration of cell number quantification and cone segment length measurement (see Extended Data Fig. 3-3). Minor effect on PR structure in 7 dpf *pdx1*$^{+/-}$ *mutant* retinas.

In addition, we also found the compositional change in MC clusters. The main clusters of MC in WT included Clusters 0, 2, and 3, while the MC in *pdx1*$^{+/-}$ *mutants* and glucose-treated *pdx1*$^{+/-}$ *mutants* lost Clusters 2 and 3, which functioned in ion transport/cellular potassium ion homeostasis/glycolytic process and circadian regulation of gene expression, respectively. Meanwhile, the proportion of Cluster 1, the marker genes of which participated in regulation of actin cytoskeleton, was greatly increased in *pdx1*$^{+/-}$ *mutants* and glucose-treated *pdx1*$^{+/-}$ *mutants*. These results suggested that the MG gradually lost its physiological function and were undergoing energy failure under hyperglycemia.

Single-cell RNA-seq identifies distinct cone states in *pdx1*$^{+/-}$ *mutants* and glucose-treated *pdx1*$^{+/-}$ *mutants*

We next wondered about the developmental relationship between Cluster 2 and 6 PRs. The expressions of cone- and rod-specific gene markers indicated that Cluster 2 and 6 cells were cones (Fig. 5*A*,*B*). The hierarchical clustering analysis showed Cluster 2 and 6 as sister terminal cluster pairs, indicating that Cluster 2 exhibited the closest transcriptome-based correlation distance to Cluster 6 than those from other clusters (Fig. 5*C*).

Considering the distinct compositions of Cluster 2 and 6 among three groups (Fig. 4*F*), it raised the possibility that increased blood glucose levels led to the transcriptomic profile

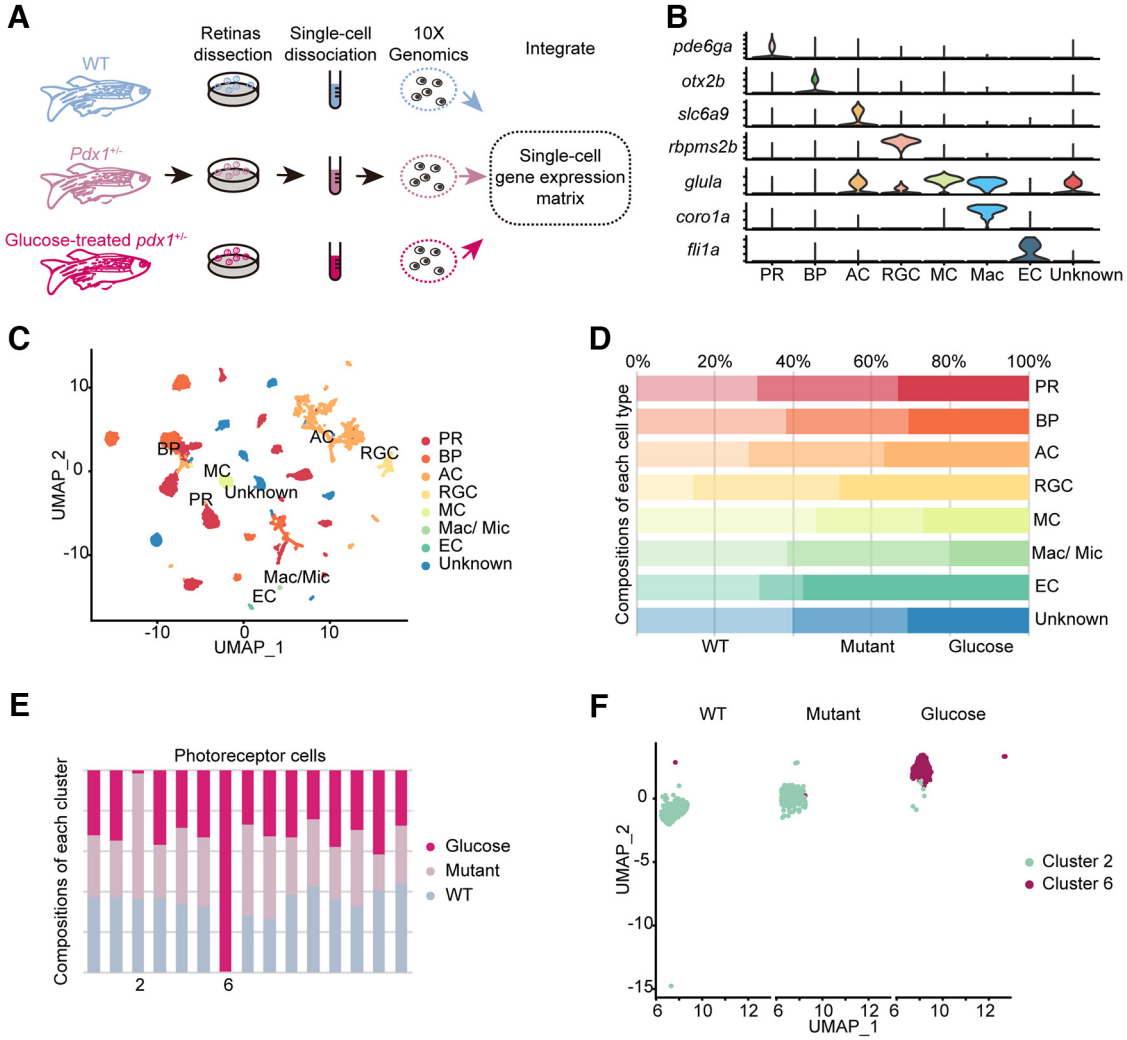

Figure 4. Changed transcriptome profiles in PR cells in single-cell RNA-seq analysis. ***A***, Experimental design of single-cell transcriptome analysis by 10× Genomics platform. WT, $n = 6$ retinas from 6 animals; *pdx1*$^{+/-}$ *mutants*, $n = 6$ retinas from 6 animals; glucose-treated *pdx1*$^{+/-}$ *mutants*, $n = 6$ retinas from 6 animals. ***B***, Relative expression of putative retinal cell type-specific gene markers in characterized cell clusters. BP, Bipolar cell; AC, amacrine cell; RGC, retinal ganglion cell; Mac, macrophage. ***C***, UMAP clustering plot of the seven cell types with an unknown type identified in all retinal cells from WT, *pdx1*$^{+/-}$, and glucose-treated *pdx1*$^{+/-}$ *mutants*. ***D***, Composition of eight cell types in WT, *pdx1*$^{+/-}$, and glucose-treated *pdx1*$^{+/-}$ *mutants*. Mutant: *pdx1*$^{+/-}$ *mutants*. Glucose: glucose-treated *pdx1*$^{+/-}$ *mutants*. WT versus *pdx1*$^{+/-}$ *mutants*, $p = 0.7$; WT versus glucose-treated *pdx1*$^{+/-}$ *mutants*, $p = 0.8$; *pdx1*$^{+/-}$ *mutants* versus glucose-treated *pdx1*$^{+/-}$ *mutants*, $p = 0.6$, by ratio paired *t* test. ***E***, Composition of PR clusters in WT, *pdx1*$^{+/-}$, and glucose-treated *pdx1*$^{+/-}$ *mutants*. ***F***, UMAP clustering plot of Cluster 2 and 6 PR cells of WT, *pdx1*$^{+/-}$, and glucose-treated *pdx1*$^{+/-}$ *mutants* (see Extended Data Fig. 4-1). Cluster compositions of major cell type in single-cell RNA-seq analysis.

transition of cones in Cluster 2 of WT and *pdx1*$^{+/-}$ *mutants* to those in Cluster 6 in glucose-treated *pdx1*$^{+/-}$ *mutants*. To test this, we performed the pseudo-time analysis of Cluster 2 and 6 cells from all three groups. The pseudo-time trajectory of Cluster 2 and 6 cells comprised three different branches representing three distinct cell states (Fig. 5*D*,*E*; States 1-3). Since State 1 cells were mainly derived from Cluster 2 cells of WT retina (85.1%), we assumed it as the root state. Thus, the pseudo-time trajectory indicated that State 1 diverged into States 2 and 3. Interestingly, Cluster 2 cells in *pdx1*$^{+/-}$ *mutants* were predominantly distributed in State 2 (78.9%) rather than State 1, where their counterparts in WT retinas were located (Fig. 5*F*). This result indicated that Cluster 2 cells in WT and *pdx1*$^{+/-}$ *mutants* were distinct in the transcriptome, suggesting a molecular transition in Cluster 2 cells from WT to *pdx1*$^{+/-}$ *mutants*. In contrast, Cluster 6 cells from glucose-treated *pdx1*$^{+/-}$ *mutants* were dominant in State 3 (91.1%) but barely in States 1 and 2 (Fig. 5*F*). Together, the change in cones between WT and *pdx1*$^{+/-}$ *mutants* mainly reflected on the transcriptomic transition of Cluster 2 cells from State 1 to State 2, whereas the cone change between *pdx1*$^{+/-}$ *mutants* and glucose-treated *pdx1*$^{+/-}$ *mutants* was represented as the difference in transcriptomic profile from Cluster 2 cells in State 2 to Cluster 6 cells in State 3.

In addition, GO analysis of differentially expressed genes among three states (States 1-3) identified molecular features of each state. State 1 was a root state preferentially expressed genes participating in retina development and transport. As to mutant-dominant states, State 2 was marked by genes enriched in the tricarboxylic acid cycle (TCA), regulation of anion transport, oxidation-reduction process, glycolytic process, and anion transport, whereas State 3 was marked by genes involved in translation and cytoplasmic translation (Fig. 5*G*). Interestingly, compared with States 1 and 2, the expression of genes related to TCA and glycolysis was significantly repressed in State 3. With higher translation-associated gene expression in State 3, our result suggested State 3 cells that mostly represented cones in Cluster 6 specific to glucose-treated *pdx1*$^{+/-}$ *mutants* were undergoing the energy failure and an elevated translation level.

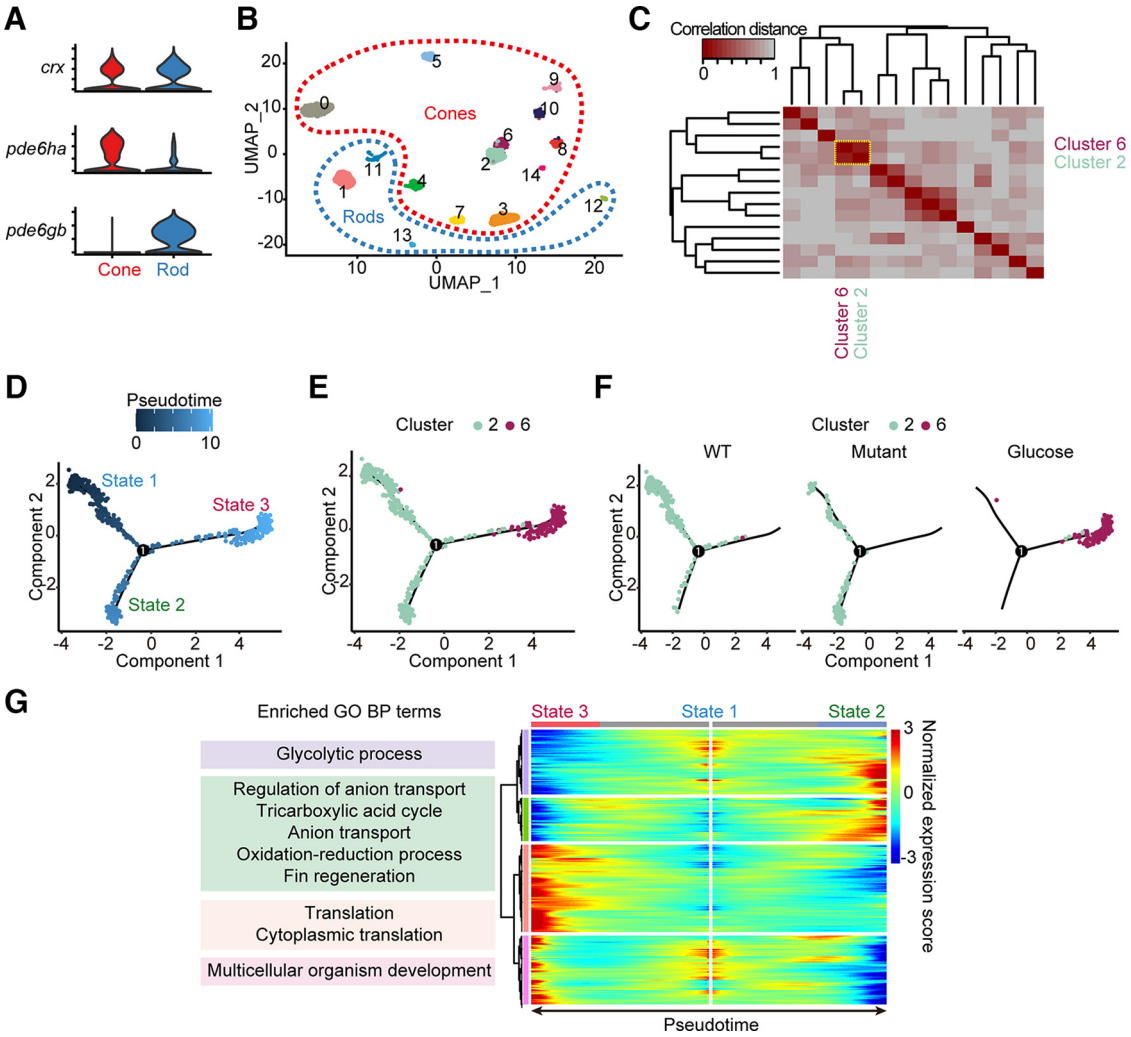

Figure 5. Distinct cone states in *pdx1*$^{+/-}$ *mutants* and glucose-treated *pdx1*$^{+/-}$ *mutants* revealed by single-cell RNA-seq analysis. ***A***, Relative expression of cone- and rod-specific gene markers in characterized PR clusters. ***B***, UMAP clustering plot of the cone and rod clusters in PRs from WT, *pdx1*$^{+/-}$, and glucose-treated *pdx1*$^{+/-}$ *mutants*. ***C***, The hierarchical clustering analysis of 15 PR clusters from WT, *pdx1*$^{+/-}$, and glucose-treated *pdx1*$^{+/-}$ *mutants*. ***D***, ***E***, The pseudo-time analysis of Cluster 2 and 6 cones from WT, *pdx1*$^{+/-}$, and glucose-treated *pdx1*$^{+/-}$ *mutants*. ***F***, The pseudo-time analysis of Cluster 2 and 6 cones in WT, *pdx1*$^{+/-}$, and glucose-treated *pdx1*$^{+/-}$ *mutants*, respectively. ***G***, Pseudo-time heatmap plot and GO analysis of differentially expressed genes among States 1-3. Differential genes: $p < 0.0001$. GO terms: $p < 0.01$.

Cone-specific *hcn1* downregulation under hyperglycemia

To explore the molecular mechanism responsible for cone structural alteration under hyperglycemia, we focused on the differentially expressed genes between State 1 and State 2/3 (Fig. 5*G*). We found that expression of cone-specific *hcn1* was significantly higher in State 1 than in State 2/3 (Fig. 6*A*,*B*; $p < 0.0001$, by one-way ANOVA). Specifically, the pseudo-time analysis showed a declined expression pattern of *hcn1*: its expression was highest in State 1 (Cluster 2, WT group), and was significantly dropped in State 2 (Cluster 2, *pdx1*$^{+/-}$ *mutants*), and reached the lowest level in State 3 (Cluster 6, glucose-treated *pdx1*$^{+/-}$ *mutants*) (Fig. 6*B*). ISH verified the cone-specific expression of *hcn1* and declined expression patterns from WT animals to *pdx1*$^{+/-}$ *mutants* and glucose-treated *pdx1*$^{+/-}$ *mutants* (Fig. 6*C*). The further quantification showed that the area fraction of *hcn1* expression in cone layers was significantly decreased in *pdx1*$^{+/-}$ *mutants* ($1.0 \pm 1.8\%$, $n = 7$ retinas from 7 animals) and glucose-treated *pdx1*$^{+/-}$ *mutants* ($0.8 \pm 0.8\%$, $n = 7$ retinas from 7 animals), compared with that of the WT group (Fig. 6*E*; WT, $3.8 \pm 1.4\%$, $n = 5$ retinas from 5 animals; WT vs *pdx1*$^{+/-}$ *mutants*, $p = 0.0014$, by two-tailed unpaired Student's *t* test; WT vs *pdx1*$^{+/-}$ *mutants* vs glucose-treated *pdx1*$^{+/-}$ *mutants*, $p = 0.0002$, by ordinary one-way ANOVA). The fluorescence intensity of *hcn1* probe signal across three groups also showed in a declined tendency, although there was no statistical significance among three groups (Fig. 6*D*; WT, 2789 ± 210.8 AU, $n = 5$ retinas from 5 animals; *pdx1*$^{+/-}$ *mutants*, 2612 ± 295.7 AU, $n = 7$ retinas from 7 animals; glucose-treated *pdx1*$^{+/-}$ *mutants*, 2521 ± 345.7 AU, $n = 7$ retinas from 7 animals; WT vs *pdx1*$^{+/-}$ *mutants* vs glucose-treated *pdx1*$^{+/-}$ *mutants*, $p = 0.3$, by ordinary one-way ANOVA). Together with the fact that the number of cones did not show significant difference among three groups (Fig. 3*A*), these results demonstrated the downregulation of *hcn1* expression in cone PR cells under hyperglycemic condition.

The downregulation of *hcn1* leads to cone morphology defects

The above results of a decreased cone-specific *hcn1* expression and cone morphologic defects in both *pdx1*$^{+/-}$ *mutants* and glucose-treated *pdx1*$^{+/-}$ *mutants* suggested the potential role of *hcn1* in maintaining normal cone morphology. To test this, we disrupted the *hcn1* gene by injecting one sgRNA targeting exon 1

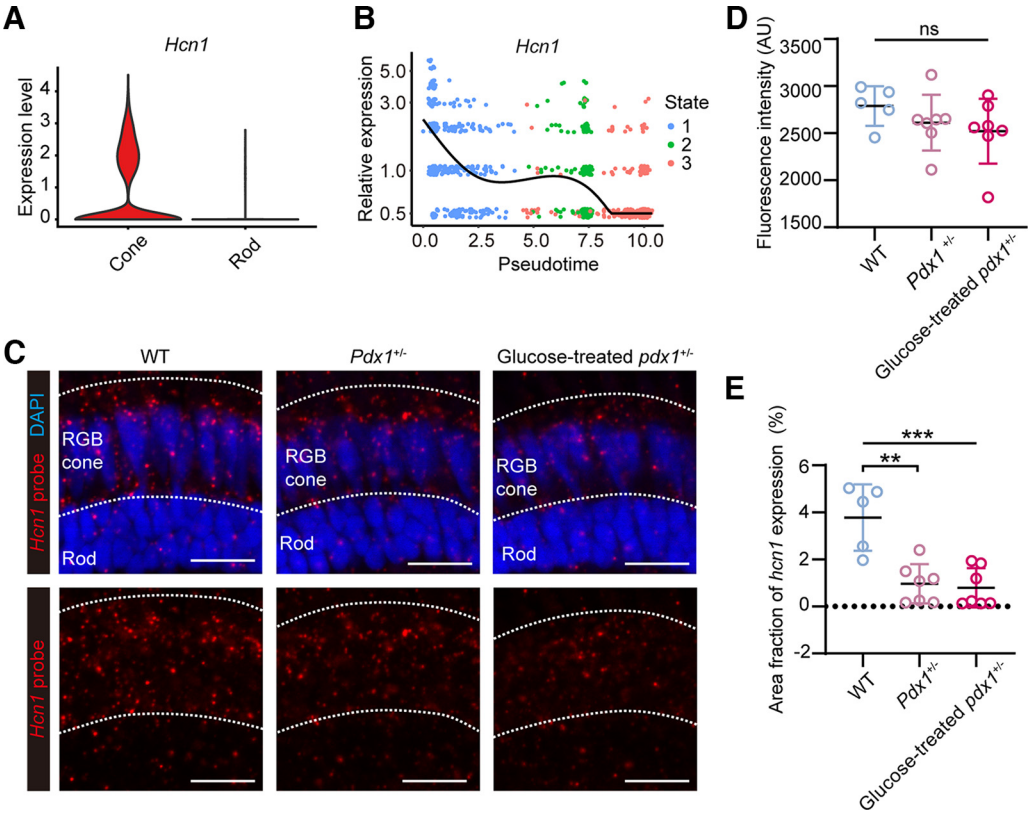

Figure 6. Progressive cone-specific *hcn1* downregulation in States 2 and 3. ***A***, Relative expression of *hcn1* in cones and rods from WT, *pdx1*$^{+/-}$, and glucose-treated *pdx1*$^{+/-}$ *mutants* by single-cell RNA-seq analysis. ***B***, The pseudo-time analysis of relative expression of *hcn1* in States 1-3 cones from WT, *pdx1*$^{+/-}$, and glucose-treated *pdx1*$^{+/-}$ *mutants*. $p < 0.0001$ (ordinary one-way ANOVA). ***C***, Representative confocal microscopic images of *hcn1* ISH in WT, *pdx1*$^{+/-}$, and glucose-treated *pdx1*$^{+/-}$ mutant retinas. Scale bars, 15 μm. The fluorescence intensity (***D***) and area fraction (***E***) of *hcn1 in situ* probe signal in 3 or more regions of cone layer per eye. Data are mean ± SD. WT, $n = 5$ retinas from 5 animals; *pdx1*$^{+/-}$ *mutants*, $n = 7$ retinas from 7 animals; glucose-treated *pdx1*$^{+/-}$ *mutants*, $n = 7$ retinas from 7 animals. $^{**}p < 0.01$ (two-tailed unpaired Student's *t* test). NS ($p > 0.05$); $^{***}p < 0.001$ (ordinary one-way ANOVA).

of the *hcn1* gene and Cas9 protein into embryos at one-cell stage. *Hcn1* has little influence on the general organization of the retina structure, as shown that the numbers of cones, rods, and the cells in INL remained unchanged (Fig. 7*A–D*). Notably, compared with the WT, the Arrestin 3-positive cones showed significantly shortened segments in 2 month *hcn1*-disrupted zebrafish retina (Fig. 7*E*,*F*; WT, 22.8 ± 4.0 μm; *hcn1 knock-outs* (KO) F0, 15.9 ± 2.6 μm, $p = 0.0004$, by two-tailed unpaired Student's *t* test). Thus, our results indicated that the loss of the *hcn1* gene could specifically disrupt the cone morphology with significantly shortened segments, recapitulating the cone phenotype in *pdx1*$^{+/-}$ *mutants* and glucose-treated *pdx1*$^{+/-}$ *mutants*.

Discussion

In this study, combining *pdx1*$^{+/-}$ zebrafish *mutants* and glucose treatment, we created a vertebrate animal model that could represent the progressive DR phenotypes, including elevated blood glucose levels, cone segment shortening, increased vessel branches, narrowing artery diameter, and increased *glut1* expression. The model showed the uncoupling appearance of retinal vascular abnormalities and cone defects. We found that cones were the most vulnerable retinal neuron types under hyperglycemia. Interestingly, we genetically defined two progressive cone states in response to different levels of hyperglycemia. Mechanistically, we found that *hcn1*, under a progressive reduction from *pdx1*$^{+/-}$ *mutants* and glucose-treated *pdx1*$^{+/-}$ *mutants*, was essential for cone morphologic integrity. Thus, our findings provided novel molecular and cellular insights into progressive cone-specific defects in DR.

Our results showed uncoupling appearance of retinal vascular abnormalities and cone defects. Truncated cone segments were observed in *pdx1*$^{+/-}$ *mutants* but not glucose-treated WT and became more significant in glucose-treated *pdx1*$^{+/-}$ *mutants*, whereas increased *glut1* expression appeared in glucose-treated WT and glucose-treated *pdx1*$^{+/-}$ *mutants* but not *pdx1*$^{+/-}$ *mutants*. Retinal vascular structural abnormalities were only shown in glucose-treated *pdx1*$^{+/-}$ *mutants*. These results indicated truncated cone segments as a result of impaired pancreas islet development and glucose treatment, while the retinal vascular abnormalities resulted from glucose treatment. It raised the complex contributors induced by intrinsic and extrinsic stimulus in DR progression. Takagi et al. (1998) showed that hypoxia upregulated glycolysis via increasing GLUT1 expression, and reduction of GLUT1 alleviates early characteristics of DR (You et al., 2017; Holoman et al., 2021). Whether extrinsic glucose treatment burdened retinal hypoxia and subsequent upregulation of *glut1* expression may be interesting to find out. On the other hand, the long-term loss of *pdx1* gene did not induce any microvascular abnormalities in young-adult *pdx1*$^{+/-}$ *mutants*, which raised another possibility about the compensatory effects under a low level of hyperglycemia. Many factors have been demonstrated deferring diabetic angiopathy, including cystatin C (CST3) and retinol-binding protein 3 (RBP3). The previous study showed that the expression of CST3 was significantly decreased in aqueous humors of DR patients and showed significantly negative correlations with DR severity and central retinal thickness (Han et al., 2022). CST3 was an active cysteine protease inhibitor, the lack of which

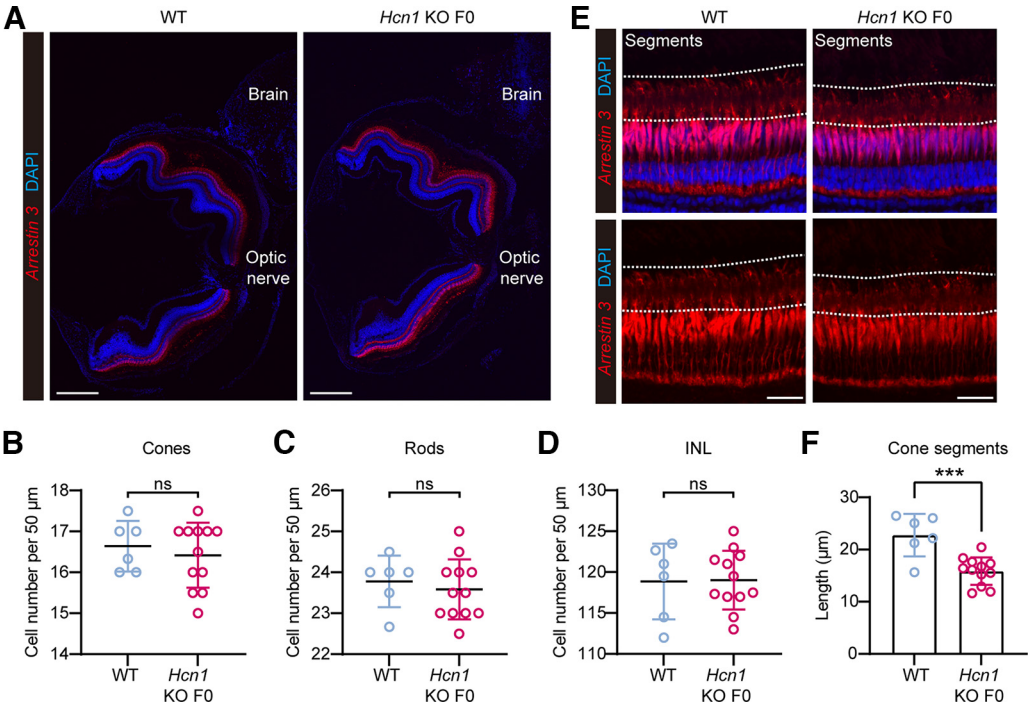

Figure 7. *Hcn1* disruption leads to cone morphologic alternation. ***A***, Representative retina structural images of WT and *hcn1* KO F0 retinas. Scale bars, 200 µm. The cell number of cones (***B***), rods (***C***), and the cells in INL (***D***) in 3 or more regions per eye. Data are mean ± SD. WT, $n = 6$ retinas from 3 animals; *hcn1* KO F0, $n = 12$ retinas from 7 animals. NS, $p > 0.05$ (two-tailed unpaired Student's *t* test). ***E***, Representative cone morphology images of WT and *hcn1* KO F0 *mutant* retinas. Scale bars, 20 µm. ***F***, The length of cone segments in 15 or more regions per eye. Data are mean ± SD. WT, $n = 6$ retinas from 3 animals; *hcn1* KO F0, $n = 12$ retinas from 7 animals. ***$p < 0.001$ (two-tailed unpaired Student's *t* test) (see Extended Data Fig. 7-1) Exemplary sequence result of mutation in *hcn1* exon 1.

promoted atherosclerosis, lamina degradation, and aortic dilatation in apolipoprotein E-deficient mice (Bengtsson et al., 2005; Sukhova et al., 2005). Importantly, reduced CST3 expression increased pro-angiogenic potential in retinal pigment epithelial cells (Carlsson et al., 2020), and pharmaceutical cysteine protease inhibitor attenuated albumin leakage into the retina (Kumar et al., 2016). In our study, we observed an increased proportion of Cluster 1 MC cells in *pdx1*$^{+/-}$ *mutants*, whose marker genes included *cst3*. Whether the expression of *cst3* in MG delays angiopathy in *pdx1*$^{+/-}$ *mutants* may be also interesting to answer.

Our single-cell RNA-seq data suggest cones as the most vulnerable retinal neuron types in response to hyperglycemia, consistent with a recent study (Niu et al., 2021). PR properties may explain its vulnerability to hyperglycemia. PRs, particularly cones, require a large amount of energy for photo-transduction (Winkler, 1981; Okawa et al., 2008; Chinchore et al., 2017; Giarmarco et al., 2020; Ingram et al., 2020). Interestingly, 80%-96% glucose in the PRs is converted into lactate by aerobic glycolysis in the cytoplasm rather than oxidative phosphorylation in the mitochondria (Winkler, 1981; Chinchore et al., 2017), indicating the lower efficiency of the conversion from glucose to ATP. Thus, PRs are vulnerable to fluctuating glucose supply levels to ensure adequate energy production. On the other hand, a higher level of aerobic glycolysis in the retina results in excessive pyruvate, which must enter the mitochondria to be oxidized in an oxygen-dependent manner. PRs consume most oxygen in the retina and process very high levels of mitochondria, particularly in cones, where the number of mitochondria is 2 or more times that of rods (Ahmed et al., 1993; D. Yu et al., 2005; Grenell et al., 2019; Giarmarco et al., 2020). The mitochondrial transport of pyruvate was essential for maintaining PR integrity (Grenell et al., 2019). Interestingly, our data showed that the expression of *mpc2* (mitochondrial pyruvate carrier 2) but not *mpc1* became largely absent from Cluster 6 cells of glucose-treated *pdx1*$^{+/-}$ *mutants*. In contrast, both genes were highly expressed in Cluster 2 cells in WT animals, suggesting that the deficit in mitochondrial pyruvate metabolism might be involved in cone morphologic alteration in our model. It raises the influence of higher glucose levels on mitochondrial pyruvate metabolism as a critical question to be addressed in the future.

The findings of cone progression through three cell states (States 1-3) raised a critical question about their potential functions. State-specific gene profiles generally suggest that State 2 expresses genes that resist the DR progression, whereas State 3 expresses genes that promote the DR. Compared with States 1 and 3, State 2 cells were highly expressed *rbp3* gene. Recent studies showed that the expression of RBP3 in retinas and vitreous humor of non-diabetes mellitus humans was much higher than that of DR patients (Garcia-Ramírez et al., 2009; Yokomizo et al., 2019). PRs secreted the majority of *Rbp3* in the retina. These RBP3 proteins could subsequently decrease MC glucose uptake by binding to GLUT1, thus blocking the detrimental effects resulting from hyperglycemia-induced MG inflammation (Yokomizo et al., 2019). Meanwhile, State 2 cells showed an increased expression of *gapdhs*, *pkma*, *aldocb*, *mdh1aa*, *idh2*, *sdhb*, *cycsb*, and *uqcrc1* genes, enriching in GO terms of glycolytic process, tricarboxylic acid cycle, and mitochondrial electron transport, indicating a state of elevated energetic metabolism, which is an expected consequence as a result of a higher glucose supply in *pdx1*$^{+/-}$ *mutants*. In contrast, the expression of these genes was significantly decreased in State 3, indicating the potential cell energy failure in cones, which might account for more severe cone deficits in glucose-treated *pdx1*$^{+/-}$ *mutants*. Furthermore, compared with States 1 and 2, State 3 was highly expressed in *hif1ab* (hypoxia-inducible factor 1 subunit α b) and *hif1al* (hypoxia-inducible factor 1

subunit α, like). HIF1A, the orthologous of zebrafish *hif1ab* and *hif1al*, has been demonstrated as one of the key factors in inducing VEGFA (vascular endothelial growth factor A) expression in DR patients' retinas and promoting angiogenesis, a well-known hallmark for DR at the late stage (Huang et al., 2015; J. Zhang et al., 2021). Thus, newly identified cone states reflect progressive influences of cone-derived signals on the retina with DR.

Our study showed a loss of *hcn1* under hyperglycemia. Previous studies have demonstrated the critical role of Ptdins (4,5)P2 in activating the HCN1 channel. Under hyperglycemia, the activation of the insulin pathway results in the conversion of Ptdins(4,5)P2 to Ptdins(3,4,5)P3 (phosphatidylinositol 3,4,5-trisphosphate), thereby leading to a decreased level of Ptdins(4,5)P2 on the membrane. Also, Ptdins(4,5)P2 acts as a ligand opening the HCN1 channel by shifting voltage-dependent channel activation toward depolarized potentials (H. Zhang et al., 2003). Thus, hyperglycemia was likely to repress the HCN1 channel opening through decreasing Ptdins(4,5)P2 level. It is worthwhile to explore the relationship between the activity of HCN1 channels and HCN1 transcriptional expression, which may bridge a potential link between a decreased *hcn1* expression and hyperglycemia. Meanwhile, our data showed that there were four *hcn1*-expressing cone clusters (Cluster 0, 2, 3, 7). However, Cluster 2, but not others, became absent from glucose-treated $pdx1^{+/-}$ *mutants* (Fig. 4*E*). This result suggested the molecular distinction of Cluster 2 cones from Cluster 0, 3, and 7. Interestingly, all three cone clusters other than Cluster 2 are highly expressed potassium and calcium ion channels, such as *slc24a2* (solute carrier family 24 member 2), *hcn2b* (hyperpolarization-activated cyclic nucleotide-gated potassium channel 2b), and *calb1* (calbindin 1). Previous studies also showed that NCKX4, encoded by SLC24A2, supported cones to function as daytime PRs and promote survival (Vinberg et al., 2017). Thus, the expression of these calcium and potassium ion homeostasis-related genes may endow cones (Cluster 0, 3, 7) with resistance to hyperglycemia, which is certainly interesting to address in the future.

In conclusion, we demonstrated that the *hcn1* loss resulted in the cone deficits for the first time. Although previous studies have convincingly demonstrated an essential role of *hcn1* in PR photo-response (Barrow and Wu, 2009; Seeliger et al., 2011; Tanimoto et al., 2012), a recent study of the mouse retina indicated that the deletion of *hcn1* alone had no adverse effect on the PR layer thickness of mice retina (Schön et al., 2016). At least two factors may account for the discrepancy between our result and previous mouse data: (1) our result indicated that the influence of *hcn1* loss is more cone-specific, which may result in more robust phenotypes in cone-dominant zebrafish retina than in rod-enriched mouse retina; and (2) in the mouse study, the author examined the cone deficits by focusing on the thickness of the PR layer, which may underscore the alternation in more refined structures, such as PR segments.

References

Ahmed J, Braun R, Dunn R, Linsenmeier R (1993) Oxygen distribution in the macaque retina. Invest Ophthalmol Vis Sci 34:516–521.

Ali Z, Zang J, Lagali N, Schmitner N, Salvenmoser W, Mukwaya A, Neuhauss S, Jensen L, Kimmel R (2020) Photoreceptor degeneration accompanies vascular changes in a zebrafish model of diabetic retinopathy. Invest Ophthalmol Vis Sci 61:43.

Alvarez Y, Chen K, Reynolds A, Waghorne N, O'Connor J, Kennedy B (2010) Predominant cone photoreceptor dysfunction in a hyperglycaemic model of non-proliferative diabetic retinopathy. Dis Model Mech 3:236–245.

Antonetti DA, Silva PS, Stitt AW (2021) Current understanding of the molecular and cellular pathology of diabetic retinopathy. Nat Rev Endocrinol 17:195–206.

Barrow A, Wu S (2009) Low-conductance HCN1 ion channels augment the frequency response of rod and cone photoreceptors. J Neurosci 29:5841–5853.

Bearse M, Adams A, Han Y, Schneck M, Ng J, Bronson-Castain K, Barez S (2006) A multifocal electroretinogram model predicting the development of diabetic retinopathy. Prog Retin Eye Res 25:425–448.

Bengtsson E, To F, Håkansson K, Grubb A, Brånén L, Nilsson J, Jovinge S (2005) Lack of the cysteine protease inhibitor cystatin C promotes atherosclerosis in apolipoprotein E-deficient mice. Arterioscler Thromb Vasc Biol 25:2151–2156.

Boynton G, Stem M, Kwark L, Jackson G, Farsiu S, Gardner T (2015) Multimodal characterization of proliferative diabetic retinopathy reveals alterations in outer retinal function and structure. Ophthalmology 122:957–967.

Bringmann A, Syrbe S, Görner K, Kacza J, Francke M, Wiedemann P, Reichenbach A (2018) The primate fovea: structure, function and development. Prog Retin Eye Res 66:49–84.

Carlsson E, Supharattanasitthi W, Jackson M, Paraoan L (2020) Increased rate of retinal pigment epithelial cell migration and pro-angiogenic potential ensuing from reduced cystatin C expression. Invest Ophthalmol Vis Sci 61:9.

Chinchore Y, Begaj T, Wu D, Drokhlyansky E, Cepko C (2017) Glycolytic reliance promotes anabolism in photoreceptors. Elife 6:e25946.

Du Y, Veenstra A, Palczewski K, Kern T (2013) Photoreceptor cells are major contributors to diabetes-induced oxidative stress and local inflammation in the retina. Proc Natl Acad Sci USA 110:16586–16591.

Eliwa T, Hussein M, Zaki M, Raslan O (2018) Outer retinal layer thickness as good visual predictor in patients with diabetic macular edema. Retina 38:805–811.

Énzsöly A, Szabó A, Kántor O, Dávid C, Szalay P, Szabó K, Szél Á, Németh J, Lukáts Á (2014) Pathologic alterations of the outer retina in streptozotocin-induced diabetes. Invest Ophthalmol Vis Sci 55:3686–3699.

Fu Z, Wang Z, Liu C, Gong Y, Cakir B, Liegl R, Sun Y, Meng S, Burnim S, Arellano I, Moran E, Duran R, Poblete A, Cho S, Talukdar S, Akula J, Hellström A, Smith L (2018) Fibroblast growth factor 21 protects photoreceptor function in type 1 diabetic mice. Diabetes 67:974–985.

Garcia-Ramírez M, Hernández C, Villarroel M, Canals F, Alonso M, Fortuny R, Masmiquel L, Navarro A, García-Arumí J, Simó R (2009) Interphotoreceptor retinoid-binding protein (IRBP) is downregulated at early stages of diabetic retinopathy. Diabetologia 52:2633–2641.

Giarmarco M, Brock D, Robbings B, Cleghorn W, Tsantilas K, Kuch K, Ge W, Rutter K, Parker E, Hurley J, Brockerhoff S (2020) Daily mitochondrial dynamics in cone photoreceptors. Proc Natl Acad Sci USA 117:28816–28827.

Greenstein V, Holopigian K, Seiple W, Carr R, Hood D (2004) Atypical multifocal ERG responses in patients with diseases affecting the photoreceptors. Vision Res 44:2867–2874.

Greenstein V, Sarter B, Hood D, Noble K, Carr R (1990) Hue discrimination and S cone pathway sensitivity in early diabetic retinopathy. Invest Ophthalmol Vis Sci 31:1008–1014.

Grenell A, Wang Y, Yam M, Swarup A, Dilan T, Hauer A, Linton J, Philp N, Gregor E, Zhu S, Shi Q, Murphy J, Guan T, Lohner D, Kolandaivelu S, Ramamurthy V, Goldberg A, Hurley J, Du J (2019) Loss of MPC1 reprograms retinal metabolism to impair visual function. Proc Natl Acad Sci USA 116:3530–3535.

Han RY, Gong RW, Liu W, Xu GZ (2022) Proteome changes associated with the VEGFR pathway and immune system in diabetic macular edema patients at different diabetic retinopathy stages. Curr Eye Res 47:1050–1060.

Holoman N, Aiello J, Trobenter T, Tarchick M, Kozlowski M, Makowski E, De Vivo D, Singh C, Sears J, Samuels I (2021) Reduction of Glut1 in the neural retina but not the RPE alleviates polyol accumulation and normalizes early characteristics of diabetic retinopathy. J Neurosci 41:3275–3299.

Huang H, He J, Johnson D, Wei Y, Liu Y, Wang S, Lutty G, Duh E, Semba R (2015) Deletion of placental growth factor prevents diabetic retinopathy and is associated with Akt activation and HIF1α-VEGF pathway inhibition. Diabetes 64:200–212.

Ingram N, Fain G, Sampath A (2020) Elevated energy requirement of cone photoreceptors. Proc Natl Acad Sci USA 117:19599–19603.
Kumagai A, Vinores S, Pardridge W (1996) Pathological upregulation of inner blood-retinal barrier Glut1 glucose transporter expression in diabetes mellitus. Brain Res 706:313–317.
Kumar VS, et al. (2016) Cathepsin S cleavage of protease-activated receptor-2 on endothelial cells promotes microvascular diabetes complications. J Am Soc Nephrol 27:1635–1649.
Lammer J, Prager S, Cheney M, Ahmed A, Radwan S, Burns S, Silva P, Sun J (2016) Cone photoreceptor irregularity on adaptive optics scanning laser ophthalmoscopy correlates with severity of diabetic retinopathy and macular edema. Invest Ophthalmol Vis Sci 57:6624–6632.
Lin J, Kubota S, Ban N, Yoshida M, Santeford A, Sene A, Nakamura R, Zapata N, Kubota M, Tsubota K, Yoshino J, Imai S, Apte R (2016) NAMPT-mediated NAD(+) biosynthesis is essential for vision in mice. Cell Rep 17:69–85.
Lombardo M, Parravano M, Lombardo G, Varano M, Boccassini B, Stirpe M, Serrao S (2014) Adaptive optics imaging of parafoveal cones in type 1 diabetes. Retina 34:546–557.
Niu T, Fang J, Shi X, Zhao M, Xing X, Wang Y, Zhu S, Liu K (2021) Pathogenesis study based on high-throughput single-cell sequencing analysis reveals novel transcriptional landscape and heterogeneity of retinal cells in type 2 diabetic mice. Diabetes 70:1185–1197.
Okawa H, Sampath A, Laughlin S, Fain G (2008) ATP consumption by mammalian rod photoreceptors in darkness and in light. Curr Biol 18:1917–1921.
Pan WW, Lin F, Fort PE (2021) The innate immune system in diabetic retinopathy. Prog Retin Eye Res 84:100940.
Park S, Park J, Park S, Kim K, Chung J, Chun M, Oh S (2003) Apoptotic death of photoreceptors in the streptozotocin-induced diabetic rat retina. Diabetologia 46:1260–1268.
Pisharath H, Rhee J, Swanson M, Leach S, Parsons M (2007) Targeted ablation of beta cells in the embryonic zebrafish pancreas using *E. coli* nitroreductase. Mech Dev 124:218–229.
Rajagopal R, Sylvester B, Zhang S, Adak S, Wei X, Bowers M, Jessberger S, Hsu F, Semenkovich C (2021) Glucose-mediated de novo lipogenesis in photoreceptors drives early diabetic retinopathy. J Biol Chem 297:101104.
Roman B, Pham V, Lawson N, Kulik M, Childs S, Lekven A, Garrity D, Moon R, Fishman M, Lechleider R, Weinstein B (2002) Disruption of acvrl1 increases endothelial cell number in zebrafish cranial vessels. Development 129:3009–3019.
Schön C, Asteriti S, Koch S, Sothilingam V, Garcia Garrido M, Tanimoto N, Herms J, Seeliger M, Cangiano L, Biel M, Michalakis S (2016) Loss of HCN1 enhances disease progression in mouse models of CNG channel-linked retinitis pigmentosa and achromatopsia. Hum Mol Genet 25:1165–1175.
Seeliger M, Brombas A, Weiler R, Humphries P, Knop G, Tanimoto N, Müller F (2011) Modulation of rod photoreceptor output by HCN1 channels is essential for regular mesopic cone vision. Nat Commun 2:532.
Stitt A, Curtis T, Chen M, Medina R, McKay G, Jenkins A, Gardiner T, Lyons T, Hammes H, Simó R, Lois N (2016) The progress in understanding and treatment of diabetic retinopathy. Prog Retin Eye Res 51:156–186.
Sukhova GK, Wang B, Libby P, Pan JH, Zhang Y, Grubb A, Fang K, Chapman HA, Shi GP (2005) Cystatin C deficiency increases elastic lamina degradation and aortic dilatation in apolipoprotein E-null mice. Circ Res 96:368–375.
Takagi H, King G, Aiello L (1998) Hypoxia upregulates glucose transport activity through an adenosine-mediated increase of GLUT1 expression in retinal capillary endothelial cells. Diabetes 47:1480–1488.
Tan W, Wright T, Rajendran D, Garcia-Sanchez Y, Finkelberg L, Kisilak M, Campbell M, Westall C (2015) Cone-photoreceptor density in adolescents with type 1 diabetes. Invest Ophthalmol Vis Sci 56:6339–6343.
Tanimoto N, Brombas A, Müller F, Seeliger M (2012) HCN1 channels significantly shape retinal photoresponses. Adv Exp Med Biol 723:807–812.
Tavares Ferreira J, Alves M, Dias-Santos A, Costa L, Santos B, Cunha J, Papoila A, Abegão Pinto L (2016) Retinal neurodegeneration in diabetic patients without diabetic retinopathy. Invest Ophthalmol Vis Sci 57:6455–6460.
Tavares Ferreira J, Proença R, Alves M, Dias-Santos A, Santos B, Cunha J, Papoila A, Abegão Pinto L (2017) Retina and choroid of diabetic patients without observed retinal vascular changes: a longitudinal study. Am J Ophthalmol 176:15–25.
Tonade D, Liu H, Kern T (2016) Photoreceptor cells produce inflammatory mediators that contribute to endothelial cell death in diabetes. Invest Ophthalmol Vis Sci 57:4264–4271.
Viets K, Eldred K, Johnston R (2016) Mechanisms of photoreceptor patterning in vertebrates and invertebrates. Trends Genet 32:638–659.
Vinberg F, Wang T, De Maria A, Zhao H, Bassnett S, Chen J, Kefalov V (2017) The Na^+/Ca^{2+}, K^+ exchanger NCKX4 is required for efficient cone-mediated vision. Elife 6:e24550.
Wanek J, Blair N, Chau F, Lim J, Leiderman Y, Shahidi M (2016) Alterations in retinal layer thickness and reflectance at different stages of diabetic retinopathy by en face optical coherence tomography. Invest Ophthalmol Vis Sci 57:OCT341–OCT347.
Wiggenhauser L, Qi H, Stoll S, Metzger L, Bennewitz K, Poschet G, Krenning G, Hillebrands J, Hammes H, Kroll J (2020) Pdx1 activation of retinal angiogenesis in hyperglycemic zebrafish *mutants*. Diabetes 69:1020–1031.
Winkler B (1981) Glycolytic and oxidative metabolism in relation to retinal function. J Gen Physiol 77:667–692.
Yokomizo H, et al. (2019) Retinol binding protein 3 is increased in the retina of patients with diabetes resistant to diabetic retinopathy. Sci Transl Med 11:eaau6627.
You ZP, Zhang YL, Shi K, Shi L, Zhang YZ, Zhou Y, Wang CY (2017) Suppression of diabetic retinopathy with GLUT1 siRNA. Sci Rep 7:7437.
Yu D, Cringle S, Su E (2005) Intraretinal oxygen distribution in the monkey retina and the response to systemic hyperoxia. Invest Ophthalmol Vis Sci 46:4728–4733.
Yu S, He J (2019) Stochastic cell-cycle entry and cell-state-dependent fate outputs of injury-reactivated tectal radial glia in zebrafish. Elife 8:e48660.
Zang L, Shimada Y, Nishimura Y, Tanaka T, Nishimura N (2015) Repeated blood collection for blood tests in adult zebrafish. J Vis Exp 102:e53272.
Zhang H, Craciun L, Mirshahi T, Rohács T, Lopes C, Jin T, Logothetis D (2003) PIP(2) activates KCNQ channels, and its hydrolysis underlies receptor-mediated inhibition of M currents. Neuron 37:963–975.
Zhang J, et al. (2021) HIF-1α and HIF-2α redundantly promote retinal neovascularization in patients with ischemic retinal disease. J Clin Invest 131:e13902.